Electronic Supplementary Information

Modulating reaction pathway of phenyl diazonium ion using host-guest complexation with cucurbit[7]uril

Suresh Moorthy[†a], Alvaro Castillo Bonillo[†ab], Hugues Lambert[ab], Elina Kalenius[c], Tung-Chun Lee[*ab]

a Institute for Materials Discovery
University College London (UCL)
London WC1H 0AJ, U.K
E-mail: tungchun.lee@ucl.ac.uk
b Department of Chemistry
University College London (UCL)
London WC1H 0AJ, U.K
c Department of Chemistry, Nanoscience Center
University of Jyväskylä
Jyväskylä, Finland.

† Authors contributed equally to this work.

S1. Materials and methods

Cucurbit[7]uril (CB7) and phenyldiazonium tetrafluoroborate ($PhN_2{\bullet}BF_4$) were prepared as reported in the literature.[S1,S2] Aniline, phenol, tetrafluoroboric acid solution (48 wt % in water), hydrochloric acid, D_2O, flurobenzne, benzene, and 2-naphthol used as supplied without further purification.

S1a. UV-vis spectroscopy. UV-vis spectra were recorded using the Flame S UV-vis ES Ocean Optics modular spectrometer attached to a DH-Mini Ocean Optics UV-vis light source.

Decomposition and photochemical decomposition of aqueous $[PhN_2]^+$ monitored by UV-vis spectroscopy. An aqueous solution of $PhN_2{\bullet}BF_4$ (1.31 mM) was freshly prepared by dissolving pure $PhN_2{\bullet}BF_4$ powder in deionized water. This solution will then be splitted into 3 individual smaller sample vials and each aged under a different condition (dark, room lighting or 254 nm UV lamp). The decomposition kinetics was monitored using UV-vis spectroscopy. See Figure S2–S5.

Diazo coupling reaction with 2-naphthol for aged sample solutions of $[PhN_2]^+$ and $[CB7\text{-}PhN_2]^+$ and product quantification by UV-vis spectroscopy. An aqueous solution of $PhN_2{\bullet}BF_4$ (1.3 mM) was freshly prepared by dissolving pure $PhN_2{\bullet}BF_4$ powder in deionized water. This solution was splitted into individual smaller sample vials (each containing 1.5 mL of sample solutions) and aged under dark condition for a specific duration of time, denoted as Δt. Similarly, another series of sample solutions were prepared by dissolving pure $PhN_2{\bullet}BF_4$ powder in an aqueous solution containing 1.5 equvalents of CB7. After a specific ageing time, diazo coupling reaction was performed by adding a homogenous solution of 2-naphthol dissolved in 5% w/w aqueous NaOH solution (2 mL, 35 mM, 35 equivalents) to the sample solutions containing $PhN_2{\bullet}BF_4$ or a mixture of CB7 and $PhN_2{\bullet}BF_4$. The resultant azo dye (Sudan I) was extracted from the aqueous phase using dichloromethane, and dried to form an bright orange powder. The obtained solid was re-dissolved in a known amount of dichloromethane to measure the concentration using UV-vis spectroscopy, by applying previously determined molar absorption coefficient (10877 $M^{-1}cm^{-1}$ at 418 nm).The dye quantification was repeated twice and the yield of extracted Sudan I was averaged from two sets of data (See Section S9).

S1b. ^{1}H NMR. ^{1}H NMR spectra for both free guests and their host-guest complexes with CB7 were collected in a brown NMR tube at ambient temperature using an AVANCE-III 400 MHz (^{1}H: 400.13 MHz) NMR instrument. The data were then processed with MestReNova software.

Determination of concentration in time-dependant ^{1}H NMR measurements: The concentration of $[PhN_2]^+$ and phenol was calculated from the total area under their NMR peaks using the formula below. In the presence of CB7, host-guest complexation kinetics for both $[PhN_2]^+$ and phenol is in the fast exchange regime and thus coalesced NMR signals of the free and complexed forms were observed. The combined concentration (free and complexed forms) of $[PhN_2]^+$ and phenol was calculated using the same formula from the total area under the coalesced signals. These concentration values were then used to find out the rate constants *k* from the first-order kinetic plots. See Figure S6–S8 for raw data and kinetics plots.

$$Concentration\ of\ a\ species = \left[\frac{Sum\ of\ area\ under\ each\ NMR\ signal\ of\ a\ species}{Sum\ of\ area\ under\ each\ NMR\ signal\ of\ reactant\ and\ product}\right] \text{ x } Initial\ Concentration\ of\ [PhN2]$$

S1c. Mass spectrometry. *Sample preparation:* 1.0 mM stock solution of CB7 and 10.0 mM of guest were prepared in LC-MS grade water. The stock solution was diluted to obtain the final concentration of 10 to 20 µM for CB7 and 2 to 5 stoichiometric equivalents of $PhN_2{\bullet}BF_4$ were then added.

Electrospray ionization (ESI) mass spectrometry experiments were carried out using Agilent 6560 ESI-IM-Q-TOF mass spectrometer equipped with dual spray ESI source. The mass spectrometer was externally calibrated with Agilent ESI tuning mix. ESI-MS experiments were carried on mass range *m/z* 50-3000. Samples were injected into the MS inlet by a direct infusion using a syringe pump and spectra were acquired using positive electrospray ionization with a flow rate of 5-10 µl/min. Heated N_2 was used as dry and nebulizer gas in the ion source. Typically following ion source parameters were used: dry gas temperature of 225 ºC, drying gas flow 3.0 L/min, nebulizer pressure 20 psi, fragmentor voltage of 400 V and capillary voltage of 4000–4500 V.

Ion-mobility mass spectrometry (IM-MS) experiments were performed using high purity N_2 as drift gas directly from a gas cylinder (purity grade 5.0). The drift tube pressure was set to 3.95 Torr and high

pressure funnel to 3.70 Torr. In the single-field IM experiments the drift tube entrance and exit voltages were set as 1700V and 224V, respectively. Trap filling time of 10 000 µs and trap release time of 350 µs were used. CCS values were determined using multifield measurements and then drift tube entrance voltage was varied from 1074 V to 1674 V with 100 V increments. Before sample introduction, ES tuning mix (Agilent Technologies) was measured as a quality control sample for CCS values.[S3,S4] Data was analyzed using MassHunter Qualitative Navigator (B.09.00) and MassHunter IM-MS Browser (Version B08.00) from Agilent Technologies, USA.

S1d. Computational details

Force-field calculations were performed using Chem3D and density functional theory (DFT) calculations were performed using Gaussian and Spartan 18 parallel suite for the wB97XD functional, and using Orca 5.0.0 for B97-3c. Restricted (close-shell) models were used in all DFT calculations.

For ground state, in the first instance, geometry optimization was performed using MMFF94, followed by full optimization using dispersion-corrected functional (wB97XD/6-31G* and then CPCM/wB97XD/6-31G*). CPCM implicit water model was employed to approximate the solvation effects in ground state calculations. Meanwhile the dispersion-corrected DFT functional wB97XD was chosen to estimate the van der Waals interactions, which are expected to contribute significantly to the stability of the host-guest complexes. Preliminary binding energy of the $[CB7\text{-}PhN_2]^+$ complex was calculated by the DFT energy of the $[CB7\text{-}PhN_2]^+$ complex minus those of CB7 and $[PhN_2]^+$.

To consolidate the preliminary computational findings, binding energies using the semiempirical PM6D3 and tight-binding method GFN2-xTB along with expensive methods such as DLPNO-CCSD(T), wB97XD/6-311+G** and HF/6-311+G** were reported in Table S2. All methods, with the exception of the van der Waals contribution-lacking HF, predicted binding energies below -15 kcal mol^{-1} which is way too strong and thus warranted the introduction of thermal corrections such as Zero Point Energy corrections and configurational entropy. After calculating the Hessians, on geometries optimised with a 10^{-7} Ha energy convergence criteria, using the GFN2-xTB method[S5] (still using the alpb solvation model) and introduction of the Rigid Rotor Harmonic Oscillator (RRHO) free energy contribution, the binding free energy of $[CB7\text{-}PhN_2]^+$ was calculated to be -4.27 kcal mol^{-1} (log$K$ = 3.1). In an attempt to characterise better the electrostatic interactions within the complex, geometries were optimised again using the B97-3c[S6] (with the CPCM solvation model) method which yielded a -17.24 kcal mol^{-1} interaction energy. Introducing the GFN2-xTB thermal contributions of 12.98 kcal mol^{-1} to the B97-3c electrostatic interactions yielded an estimated binding free energy of -4.26 kcal mol^{-1} which is very close to the binding affinity based on GFN2-xTB only.

These binding free energy estimates were compared with the predictions for protonated aniline for which the binding constant with CB7 has been experimentally measured (log$K$ = 6.63). Using GFN2-xTB only and taking into account the electrostatic, solvation and thermal contributions, after optimisation of the geometries up to a 10^{-7} Ha energy threshold, we obtained a binding free energy of -9.42 kcal mol^{-1} (log$K$ = 6.82) which is in excellent agreement with the experimental data. Using electrostatic and solvation contributions from B97-3c at B97-3c optimised geometries (-22.39 kcal mol^{-1}) and the GFN2-xTB thermal contributions (15.15 kcal mol^{-1}), we obtained a binding free energy of -7.24 kcal mol^{-1} (log$K$ = 5.24).

Prediction of UV-vis spectrum of $[PhN_2]^+$ was performed using the in-built function in Spartan 18 parallel suite based on time-dependent DFT (TD DFT). The optimized molecular geometry was used as the input and the TD DFT was performed at the same level of theory of the optimization.

For the transition state of $[PhN_2\text{-}H_2O]^+$, geometry search was performed by first calculating the energy profile across the increase in bond length of the C-N bond at wB97XD/6-31G* level of theory. Full transition state optimization was then performed using the Hessian approach with input geometry corresponding to the ones close to the energy maximum of the energy profile. Various input geometries were used to verified the obtained transition state. Subsequently, frequency calculation was performed at the same level of theory. The identified transition state was confirmed by the presence of one and only one vibrational mode with imaginery frequency and that the vibrational mode involves the motion of atoms resembling the bond cleavage of interest. Finally intrinsic reaction coordinate (IRC) calculation was performed to further validate and visualize the reaction mechanism. Configurational entropy was extracted from the frequency calculation.

For the transition state of $[CB7\text{-}PhN_2\text{-}H_2O]^+$, geometry search was performed by "docking" the transition state of $[PhN_2\text{-}H_2O]^+$ into CB7 using constrainted optimisation at wB97XD/6-31G* level of theory, where bond lengths of the transitional bonds (C-N and C-O) around the reaction centre were fixed. Subsequently, full optimization to transition state without any constraint was performed using the Hessian approach. Frequency calculation was performed at the same level of theory. The identified transition state was confirmed by the presence of one and only one vibrational mode with imaginery frequency and that the vibrational mode involves the motion of atoms resembling the bond cleavage of interest. Configurational entropy was extracted from the frequency calculation.

For the transition state of $[PhN_2\text{-}H_2O]^+$ in a solvent cage of explicit water molecules, 84 water molecules were randomly placed around the transition state of $[PhN_2\text{-}H_2O]^+$. The number of water molecules was chosen to be equal to the number of heavy atoms of CB7, so that differences due to charge delocalization via electrostatic induction effects can be minimized. The water molecules were relaxed at wB97XD/6-31G* level of theory with bond lengths of the transitional bonds (C-N and C-O) around the reaction centre being fixed. Subsequently, full optimization to transition state without any constraint was performed using the Hessian approach. Frequency calculation was performed at the same level of theory. The identified transition state was confirmed by the presence of one and only one vibrational mode with imaginery frequency and that the vibrational mode involves the motion of atoms resembling the bond cleavage of interest. Configurational entropy was extracted from the frequency calculation.

It should be noted that DFT computations of activation barriers can suffer from absolute errors as high as 5 kcal mol^{-1}. In the present case, the absolute values of the barrier heights are not the primary target but rather the difference between the activation energy for the solvated $[PhN_2\text{-}H_2O]^+$ and $[CB7\text{-}PhN_2\text{-}H_2O]^+$. Such difference between absolute values can be expected to benefit form a degree of error cancellation and underpins the excellent agreement between the computed increase in activation barrier and the experimentally observed decrease in the reaction rate of PhN_2^+ while in CB7.

S2. UV-vis absorption of $[PhN_2]^+$ and its photochemical decomposition in water

S2a. Experimental and calculated UV-vis spectra of $[PhN_2]^+$ ions

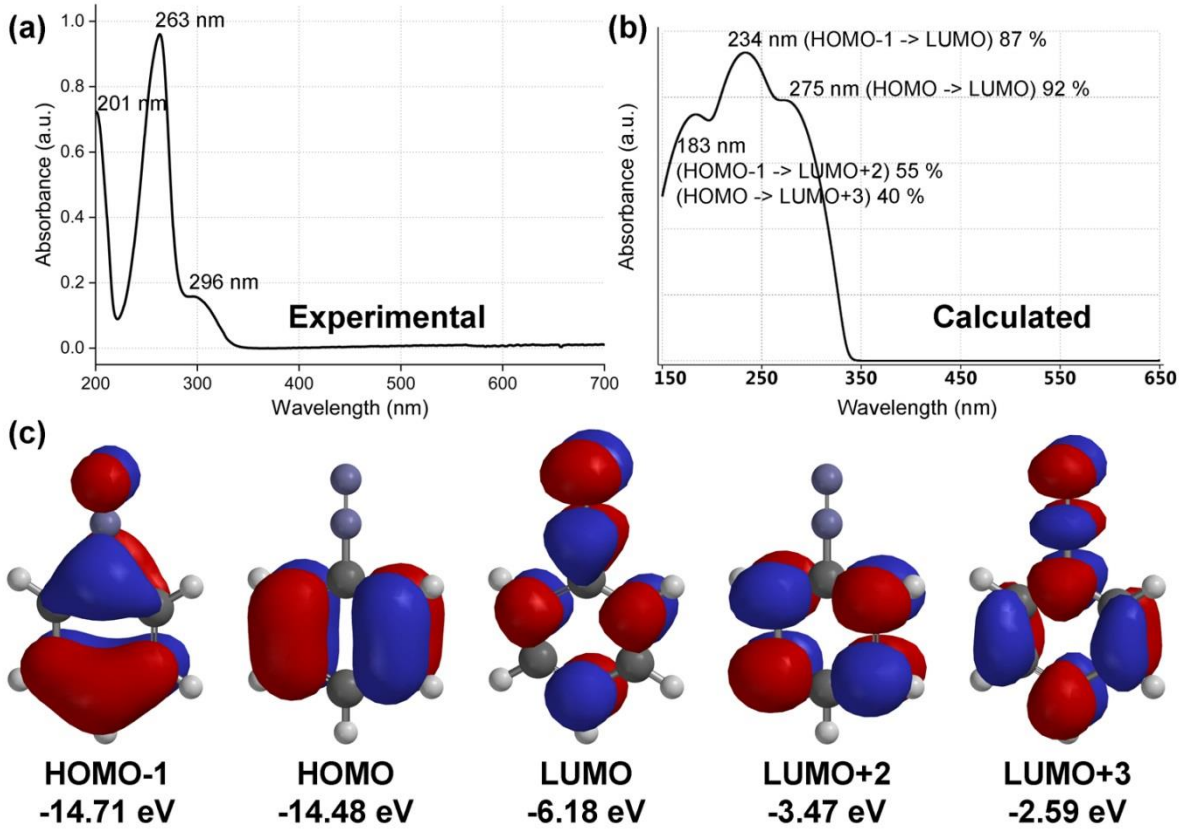

Figure S1. (a) Experimental UV-vis spectrum of a freshly prepared aqueous solution of $PhN_2{\bullet}BF_4$ (1.31 mM). **(b)** Calculated UV-vis spectrum of a $[PhN_2]^+$ ion in vacuum at wB97XD/6-31G* level of theory, where the major electronic transitions match well with the experimental observation. The slight blue shift with respect to the experimental spectrum can be attributed to the absence of solvatochromism in the modelling. **(c)** Molecular orbitals involved in the observed UV-vis electronic transitions. It is noted that the LUMO+3 exhibits an antibonding character across the C-N bond of the diazonium moiety. Thus the HOMO -> LUMO+3 transition at 183 nm, which corresponds to the experimentally observed absorption band at 201 nm, could play a major role in the UV activated dediazoniation reaction.

S2b. Time-dependant UV-vis spectra of $[PhN_2]^+$ in water under dark condition

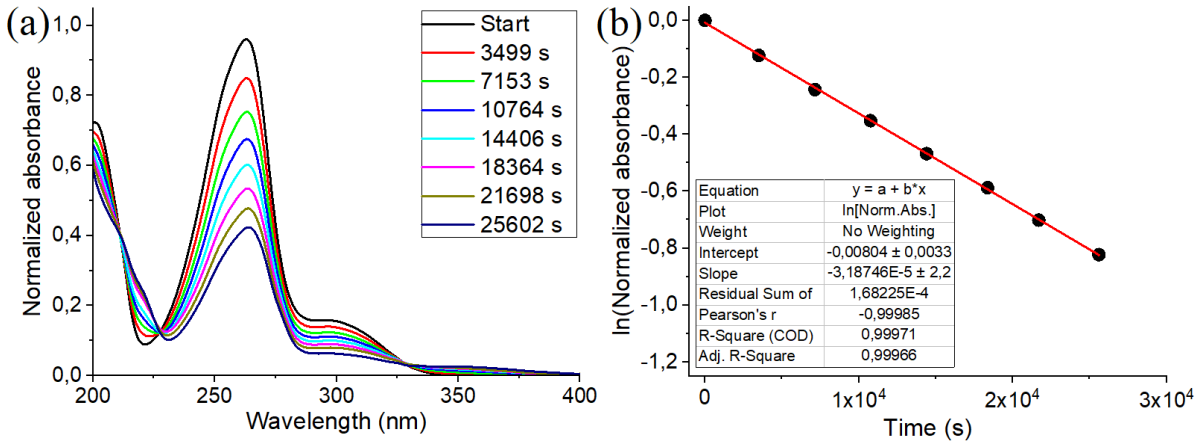

Figure S2. Decomposition of $[PhN_2]^+$ in water under dark condition monitored by UV-vis spectroscopy. **(a)** UV-vis spectra of an aqueous solution of $PhN_2{\bullet}BF_4$ (initial concentration = 1.31 mM) under dark condition as a function of time. **(b)** The corresponding first order kinetics plot of ln(normalized absorbance) against time confirming the expected S_N1(Ar) kinetics. Linear fitting parameters are shown in the inset.

S2c. Time-dependant UV-vis spectra of $[PhN_2]^+$ in water under room lighting condition

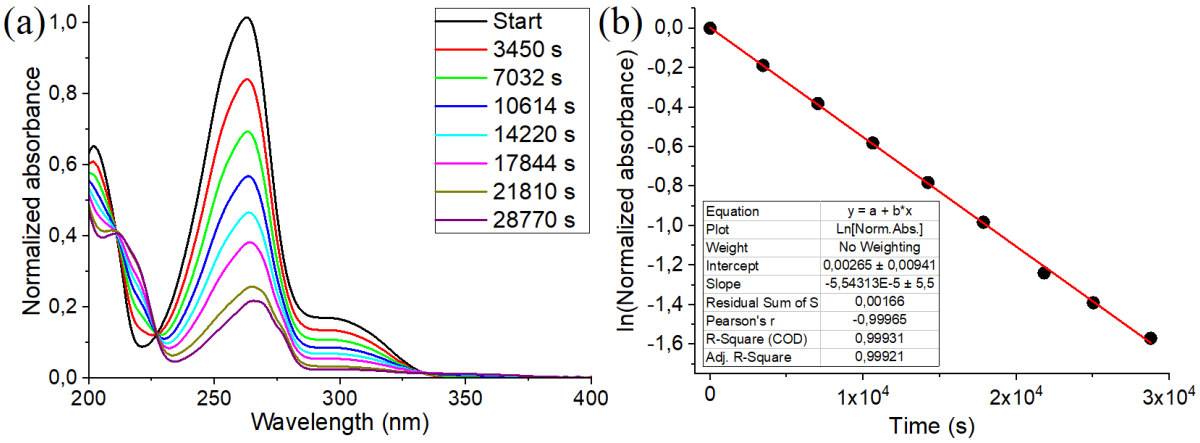

Figure S3. Decomposition of $[PhN_2]^+$ in water under room lighting condition monitored by UV-vis spectroscopy. **(a)** UV-vis spectra of an aqueous solution of $PhN_2{\bullet}BF_4$ (initial concentration = 1.31 mM) under room lighting condition as a function of time. **(b)** The corresponding first order kinetics plot of ln(normalized absorbance) against time confirming that the decompotion occurred mainly via the expected S_N1(Ar) kinetics, but with an enhanced rate constant compared to the case under dark condition. Linear fitting parameters are shown in the inset.

S2d. Time-dependant UV-vis spectra of $[PhN_2]^+$ in water when exposed to a 254 nm UV lamp

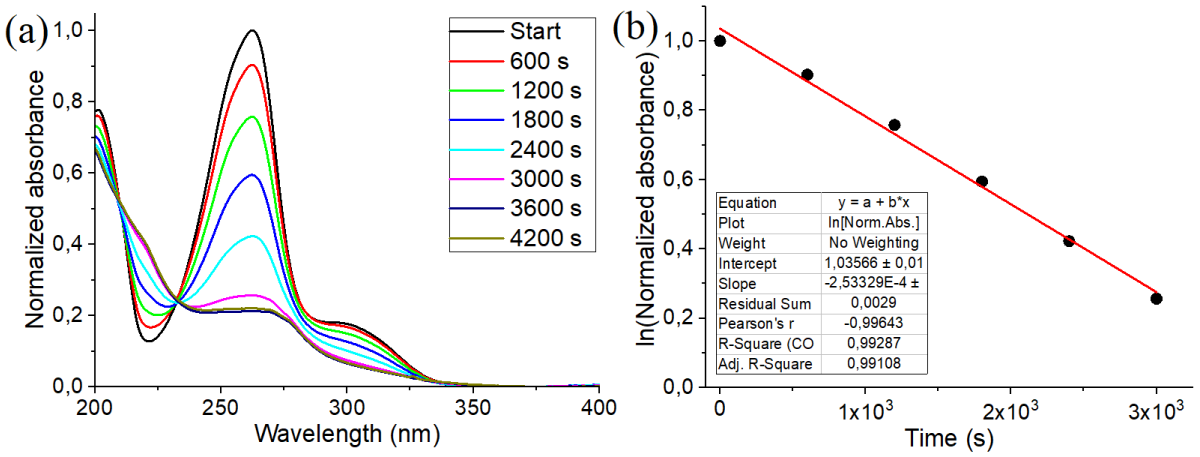

Figure S4. Decomposition of $[PhN_2]^+$ in water when exposed to a broadband UV lamp with maximum emission at 254 nm (power = 6 W) monitored by UV-vis spectroscopy. **(a)** UV-vis spectra of an aqueous solution of $PhN_2{\bullet}BF_4$ (initial concentration = 1.31 mM) under UV irradiation as a function of time. **(b)** The corresponding zeroth order kinetics plot of normalized absorbance against time confirming that the decompotion occurred mainly via the expected zeroth order kinetics of photochemical decomposition. Linear fitting parameters are shown in the inset.

S2e. Comparison linear plots under different light exposure conditions

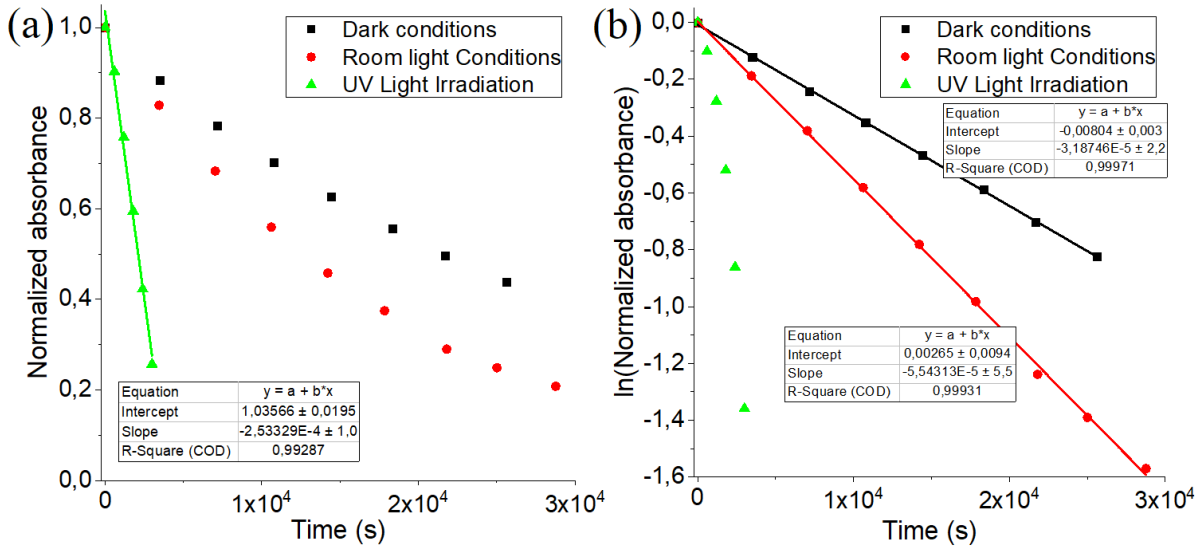

Figure S5. Comparison $[PhN_2]^+$ decomposition trends under different light exposure conditions monitored by UV-vis spectroscopy. **(a)** Normalized absorbance vs time, and **(b)** ln(normalized absorbance) vs time. Linear fitting parameters are shown in the inset.

S3. Time-dependant ^{1}H NMR spectra of $[PhN_2]^+$ and $[CB7\text{-}PhN_2]^+$ in D_2O under dark condition

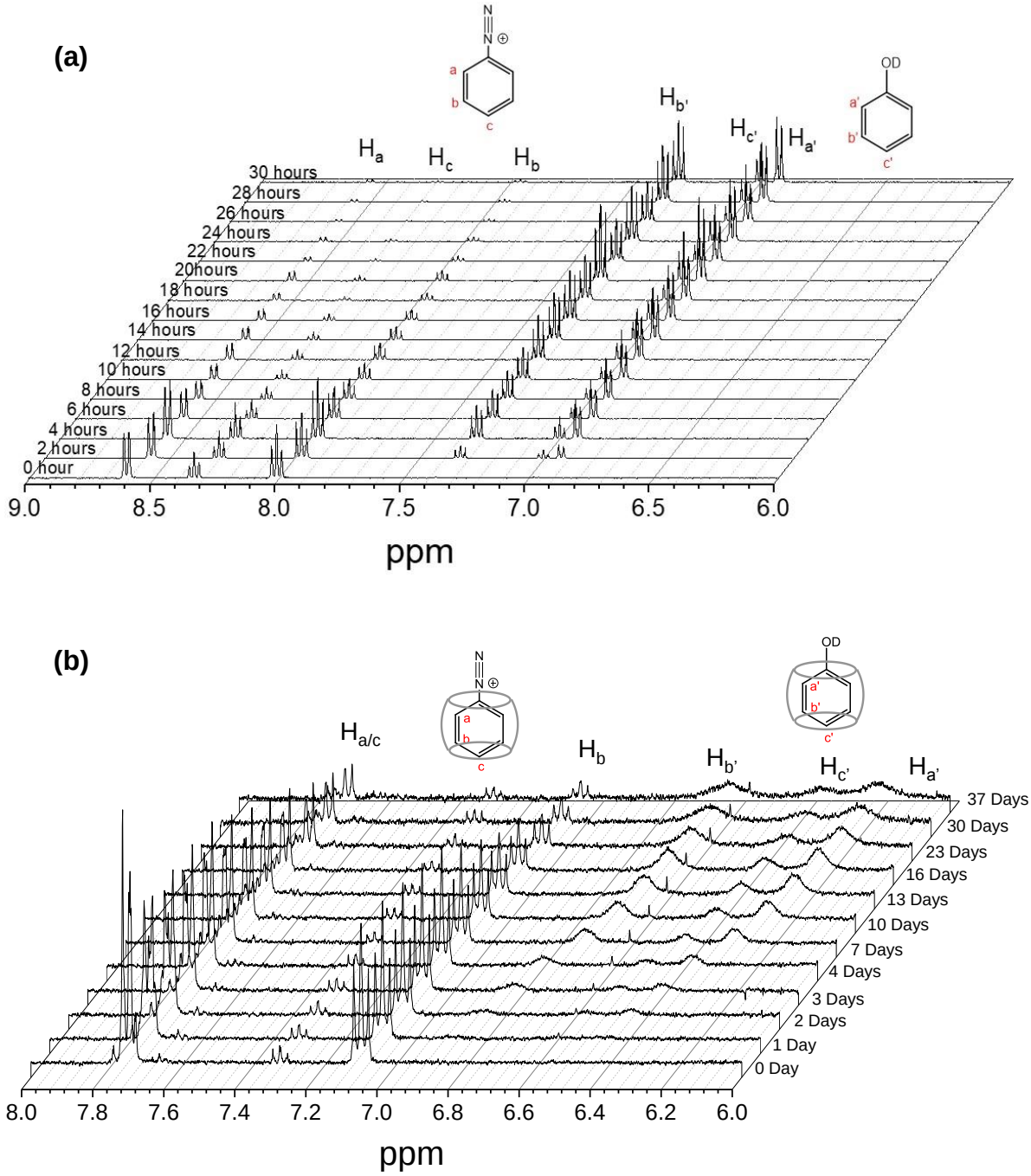

Figure S6. Time-dependant ^{1}H NMR spectra of **(a)** $PhN_2{\bullet}BF_4$ (10.0 mM) in D_2O over 30 hours, and **(b)** a mixture of CB7 (6.2 mM) and $PhN_2{\bullet}BF_4$ (4.0 mM) in D_2O over 37 days. The samples were prepared in a brown NMR tube and stored under dark condition to minimize photochemical decomposition of $[PhN_2]^+$ ions. It is noted that in (b), the peak at 7.3 ppm should be attributed to impurity, as it does not change in chemical shift and in intensity over the course of the experiment, whereas the peak at 6.6 ppm should be assigned to CB7-encapsulated benzene which formed as a minor side product (see Figure S13 for ex situ verification).

S4. Decomposition kinetics plots of $[PhN_2]^+$ and $[CB7\text{-}PhN_2]^+$ under dark condition monitored by ^1H NMR

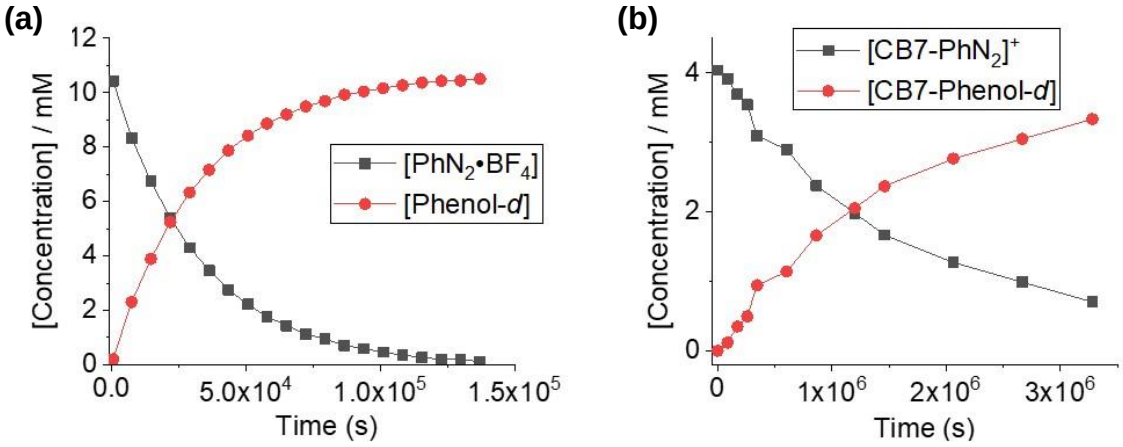

Figure S7. Decomposition kinetics of free $[PhN_2]^+$ and its CB7 complex monitored by ^1H NMR measurement (Raw data shown in Figure S6). The plots show the change in concentration of reactant and product as function of time for **(a)** free $PhN_2•BF_4$ (initial concentration = 10 mM) and **(b)** a mixture of $PhN_2•BF_4$ (initial concentration = 4.0 m M) and CB7 (initial concentration = 6.2 mM) measured in D_2O in a brown NMR tube.

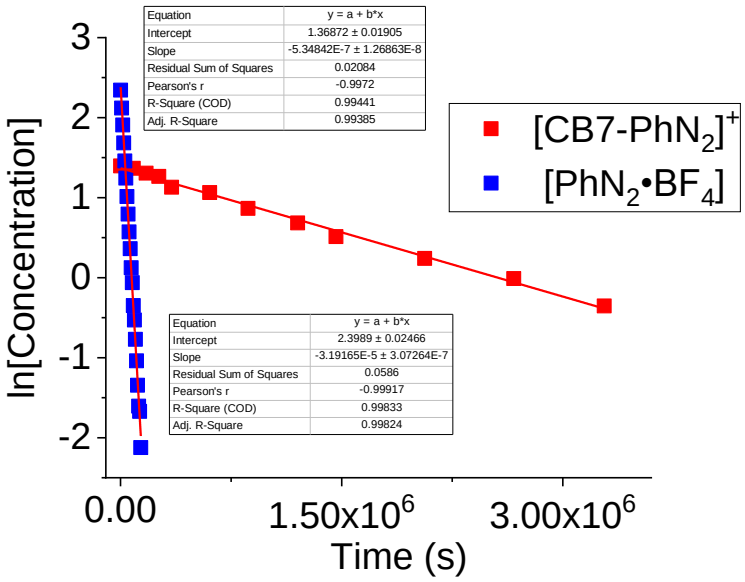

Figure S8. First order kinetics plots of ln[concentration] against time for free $[PhN_2]^+$ and $[CB7\text{-}PhN_2]^+$ under dark condition as monitored by ^1H NMR shown in Figure S6, S7. Strong linear correlations (R^2 > 0.99) in both cases confirm the expected $S_N1(Ar)$ mechanism, which is also supported by computational modelling results. Linear fitting parameters are shown in the inset where rate constant k = – slope of the linear fit. Note: This plot is the same as that in Figure 3b in the main text, except that it includes fitting parameters in the inset.

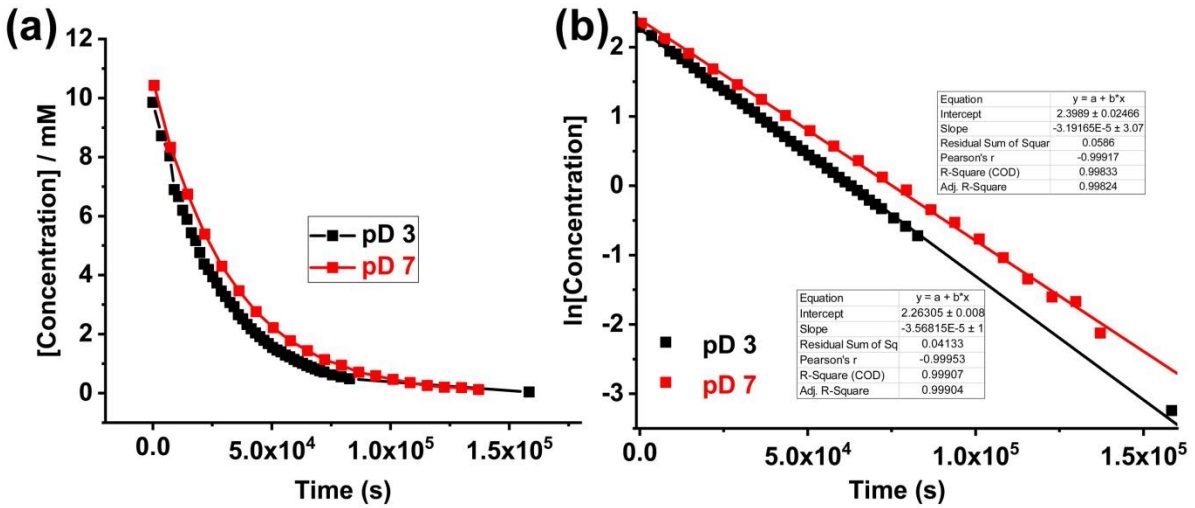

Figure S9. Decomposition kinetics of free $[PhN_2]^+$ (initial concentration = 10 mM) at pD = 3 and pD = 7 monitored by ^{1}H NMR measurement. **(a)** The plots show the change in concentration of $[PhN_2]^+$ as function of time. **(b)** Corresponding first order kinetics plots of ln[concentration] against time. Strong linear correlations (R^2 > 0.99) confirm the expected S_N1(Ar) mechanism. Linear fitting parameters are shown in the inset where rate constant k = – slope of the linear fit. The obtained half-life of $[PhN_2]^+$ at pD = 3 is 0.23 days which is consistent with the half-life at pD = ca. 7 (i.e. 0.25 days), indicating that the rate of the reaction is practically pH-independent in the pH range of our work. The slight decrease in half-life at pD = 3 can be attributed to the partial displacement of $[BF_4]^-$ by the Cl^- anions which formed the less stable $[PhN_2]^+Cl^-$, as expected. Note that the pH value of 1 mM CB7 solution prepared using deionised water and the same batch of CB7 as used in other kinetics study of our work is measured to be 5.31 ($[H^+]$ = 4.9 µM). In the kinetics study, the concentration of CB7 is 6.2 mM which corresponds to a pH value of ca. 4.52 ($[H^+]$ = 30.4 µM).

S5. Mass spectrometry of $[PhN_2]^+$ and $[CB7\text{-}PhN_2]^+$

ESI-MS mass spectra measured from sample solution containing CB7 and phenyl diazonium showed peaks corresponding to phenylium (Ph^+) complex as most abundant peak. Only a small peak corresponding to PhN_2^+ complex with CB7 was observed at *m/z* 634. In addition, peak for $[CB7+Ph+H]^{2+}$ was observed at *m/z* 620. Abundance of $[CB7+Ph+H]^{2+}$ compared to $[CB7+PhN_2+H]^{2+}$ is 27.4 fold. All complexes were observed as doubly charged ions, which is typical for CB7 complexes. Also singly charged ions for Ph^+ and PhN_2^+ are observed in mass spectrum, where the abundance of Ph^+ is 12.0 fold compared to PhN_2^+. All ions related to relevant complexes are presented in Table S1.

Ion mobility mass spectrometry measurements (IM-MS) show very similar drift times and collision cross section values ($^{DT}CCS_{N2}$) for ions $[CB7+2H]^{2+}$ (23.0 ms, 334.7 Å^2), $[CB7+PhN_2+H]^{2+}$ (23.2 ms, 337.8 Å^2) and $[CB7+Ph+H]^{2+}$ (23.2 ms, 338.9 Å^2). This confirms inclusion complexation for all host-guest complexes. Arrival time distributions for selected peaks are shown in Figure S10.

When phenyl diazonium (without CB7) is measured in water, also there $[Ph]^+$ at *m/z* 77 is observed as a base peak (abundance compared to PhN_2^+ is 27.6 fold). Careful examination of ion intensities reveals that in presence of CB7 slightly more abundant peaks for intact phenyl diazonium (PhN_2^+ and $[CB7+PhN_2+H]^{2+}$) are observed.

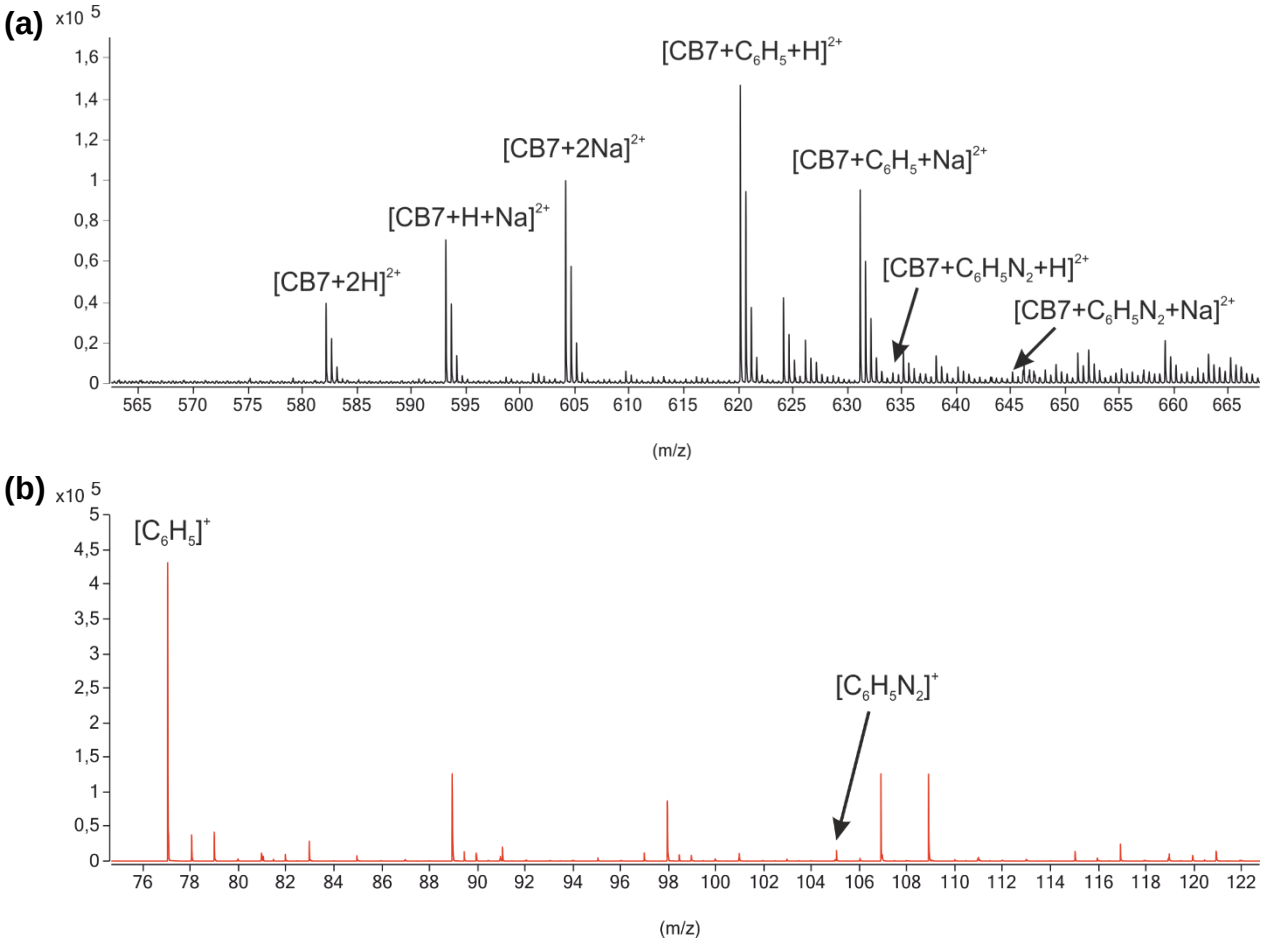

Figure S10. ESI(+) Q-TOF mass spectra for **(a)** the mixture of $PhN_2{\bullet}BF_4$ (50.0 µM) and CB7 (20.0 µM) and **(b)** $PhN_2{\bullet}BF_4$ in water containing 0.2% formic acid.

Table S1. ESI-MS data for samples containing **(a)** CB7 and $[PhN_2]^+$ and **(b)** only $[PhN_2]^+$. Table shows experimental and theoretical *m/z* values, absolute mass accuracy and relative abundances of ions.

sample	ion	*m/z* (theor)	*m/z* (exp)	mDa	%	drift time (ms)	CCS (Å^2)
(a) CB7 + $[PhN_2]^+$	$[CB7+PhN_2+H]^{2+}$	634.1978	634.1915	6.3	1.4	23.2	337.8
	$[CB7+Ph+H]^{2+}$	620.1947	620.1971	-2.4	38.4	23.2	338.9
	$[CB7+Ph+Na]^{2+}$	631.1857	631.1879	-2.2	24.8	23.2	338.6
	$[PhN_2]^+$	105.0447	105.0437	1.0	2.6	-	-
	$[Ph]^+$	77.0386	77.0382	0.4	31.3	-	-
(b) only $[PhN_2]^+$	$[PhN_2]^+$	105.0447	105.0438	0.9	3.5	-	-
	$[Ph]^+$	77.0386	77.0385	0.1	96.5	-	-

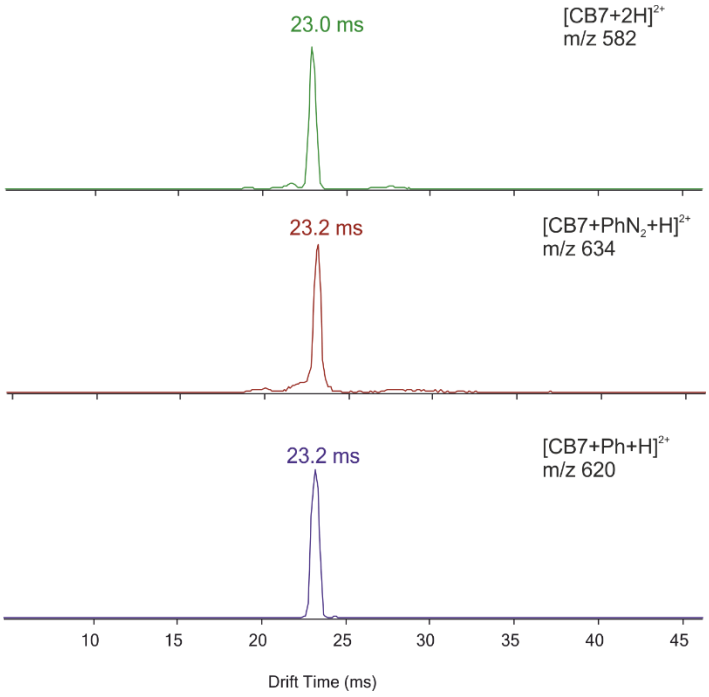

Figure S11. ESI-IM-MS arrival time distributions for selected peaks.

S6. ^{1}H NMR spectra at different $[PhN_2]^+$/CB7 ratios

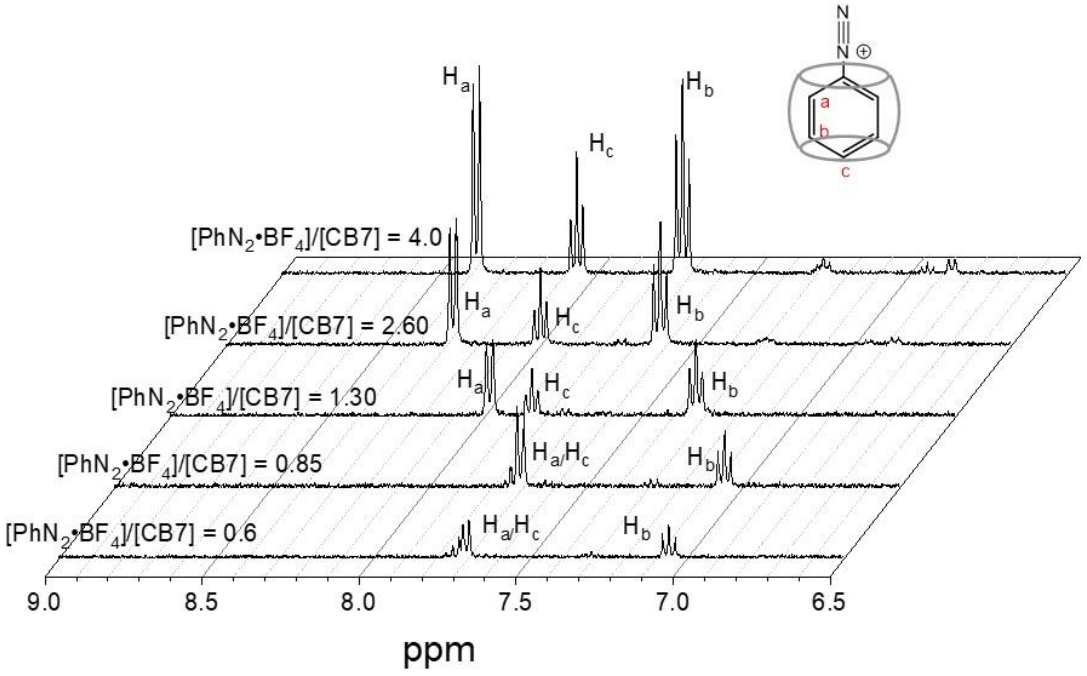

Figure S12. ^{1}H NMR spectra of mixtures containing $PhN_2•BF_4$ and CB7 at different ratios in D_2O. The spectra were measured within 30 min of sample preparation to minimize decomposition of diazonium ions. Concentration of CB7 was kept at 1.95 mM.

Driving forces of the host-guest complexation can be attributed to a combination of electrostatic interactions between the positively charged diazonium head group and the electron-rich CB7 portal, hydrophobic effects of the phenyl moiety and the release of high-energy water from the CB7 cavity. Despite various attempts, we were unable to precisely extract the binding constant of $[CB7\text{-}PhN_2]^+$ complexes using UV-vis or NMR titrations due to the chemical instability of $[PhN_2]^+$ ions in aqueous media. In light of this observation, the reliability of the reported binding constant between CB7 and 4-nitrophenyldiazonium determined using isothermal titration calorimetry,[S7] which typically takes 4 hours to complete, remains questionable. Nevertheless, the binding constant of $[CB7\text{-}PhN_2]^+$ complexes is expected to be comparable to but weaker than that between CB7 and protonated aniline ($\log K$ = 6.63),[S8] which has a similar molecular structure and the same electrostatic charge. In contrast to the case of protonated aniline, there is no hydrogen bond between the N_2-head group of $[PhN_2]^+$ and the CB7 portal and thus we expect a weaker binding for $[CB7\text{-}PhN_2]^+$ complexes, which was indeed supported by our computational study (See Section S1d).

For the association-dissociation kinetics, the $[CB7\text{-}PhN_2]^+$ system resides in the fast-exchange regime at room temperature with respect to the measurement time frame of a 400 MHz NMR instrument, as evident by the coalesced NMR signals of the $[PhN_2]^+$ protons with their chemical shifts dependent on the host-guest ratios.

S7. ^{1}H NMR spectra of CB7 complexes with possible reaction products

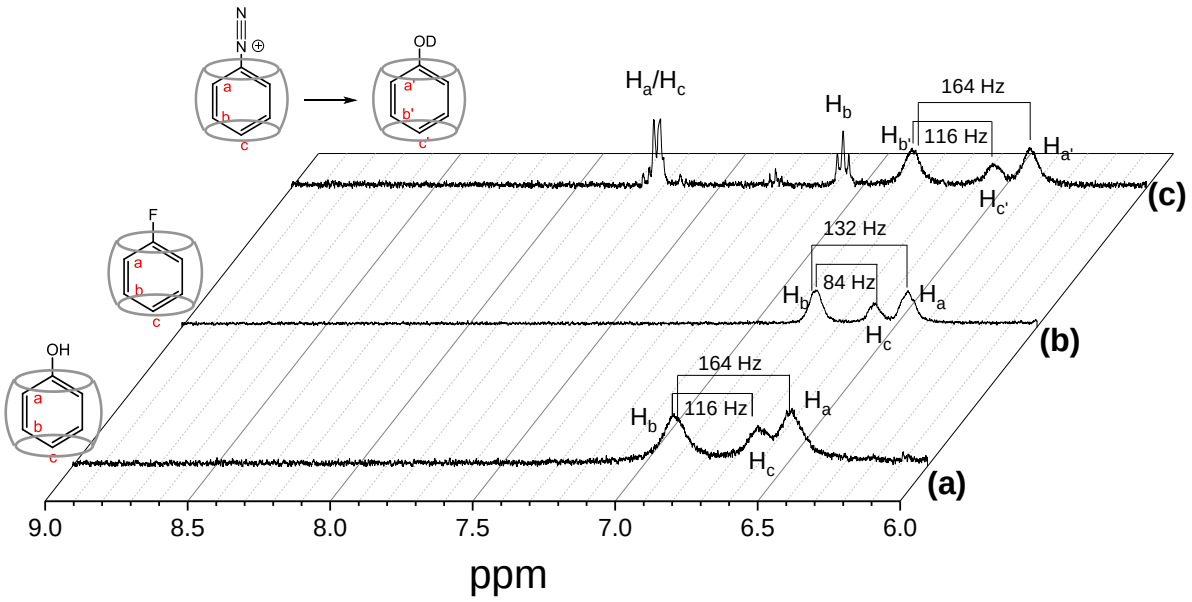

Figure S13. ^{1}H NMR spectra (400 MHz) of CB7 complexes with **(a)** phenol and **(b)** fluorobenzene prepared ex situ using 5.0 mM CB7. (c) ^{1}H NMR spectrum of a 10-day aged reaction mixture of CB7 (6.2 mM) and $PhN_2{\bullet}BF_4$ (4.0 mM) in D_2O. The ex situ measurement data confirms that phenol is the main product of the reaction and the formation of fluorobenzene has been ruled out.

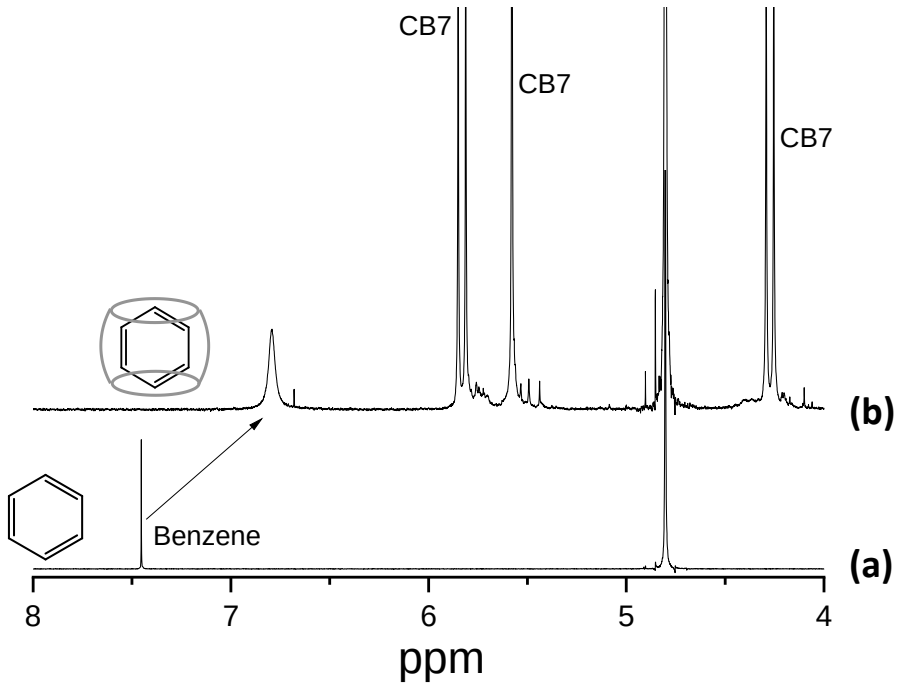

Figure S14. ^{1}H NMR spectra (400 MHz) of **(a)** free benzene and **(b)** its 1:1 complex with CB7 (5.0 mM) in D_2O. This ex situ measurement data supports the formation of benzene as a minor side product in the presence of CB7, as evident by the singlet at ~6.6ppm which is also observed in the ^{1}H NMR of the aged reaction mixture (Figure S6).

S8. Computational modelling

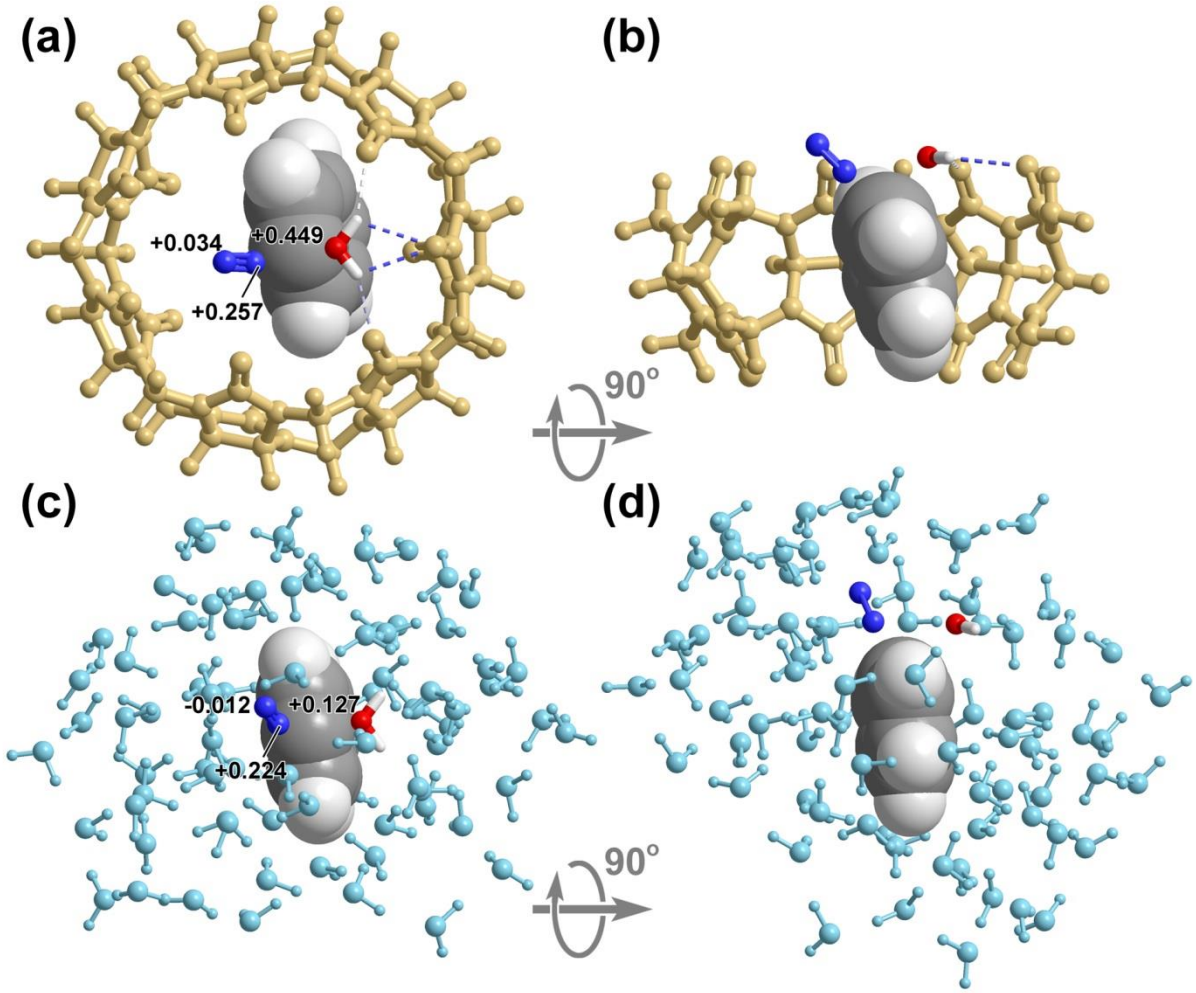

Figure S15. Transition state model of $[CB7\text{-}PhN_2\text{-}H_2O]^+$ at wB97XD/6-31G* level of theory, **(a)** top and **(b)** side views. Part of the CB7 framework is hidden for an unobstructed view of the encapsulated guest. Electrostatic partial charges are shown for selected atoms involved in the S_N1 reaction. Transition state molecular model of $[PhN_2\text{-}H_2O]^+$ in a solvent cage of 84 explicit water molecules optimized at wB97XD/6-31G* level of theory, **(c)** top and **(d)** side views. Electrostatic partial charges of the diazonium group and the α-carbon are shown as annotation. The number of water molecules was chosen to be equal to the number of heavy atoms of CB7, so that differences due to charge delocalization via electrostatic induction effects can be minimized.

It is noted that the partial charge on the α-carbon is significantly less positive when the $[PhN_2\text{-}H_2O]^+$ is in a solvent cage. This pheomenon can be attributed to the charge delocalization effects via dipole-induced dipole interactions between the phenyl ring and the surrounding water molecules, stabilizing the transition state. In contrast, the positively charged phenyl ring is not effectively stabilized by ion-induced dipole interactions in the CB7 cavity which exhibits an exceptionally low dielectric constant due to the fact that all electron lone pairs on CB7 are pointing outwards.

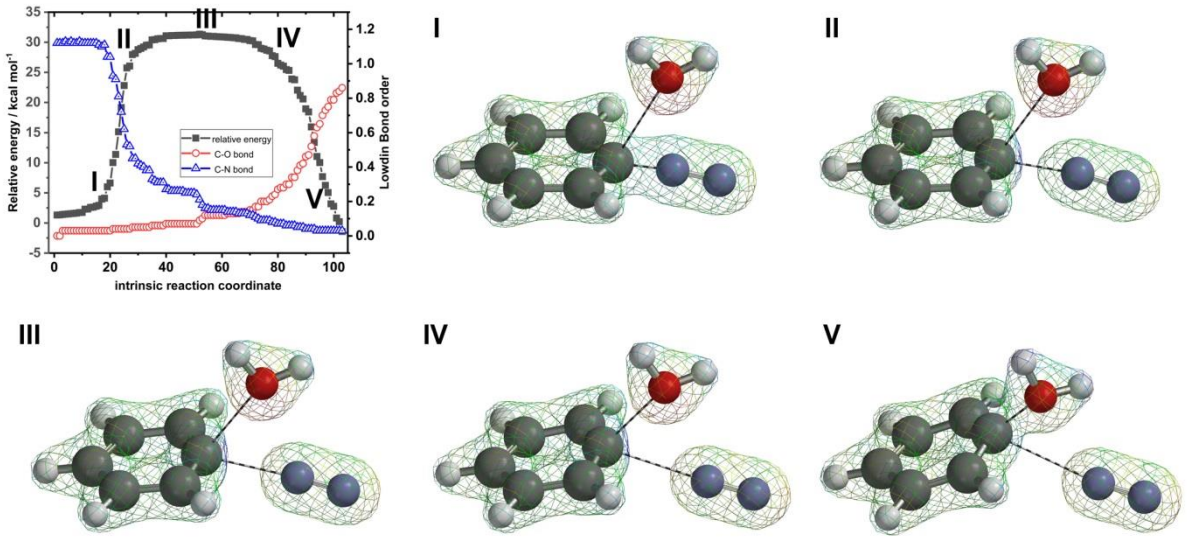

Figure S16. Intrinsic reaction coordinate (IRC) analysis of $[PhN_2\text{-}H_2O]^+$ at wB97XD/6-31G* level of theory. Profiles of relative energy and Löwdin bond orders of C-O and C-N bonds around the transition state are plotted in the top left panel, while representative geometries (denoted as **I** – **V**) are marked on the plot and visualized as individual panels. Electrostatic potential surfaces are depicted in wireframes (blue: most positive, green: medium, and red: most negative).

The transition state model (**III**) and IRC calculation support the expected S_N1(Ar) mechanism. In particular, at the transition state, significant localization of the positive charge (blue) on the α-carbon is observed, giving rise to a carbocation-like species. Meanwhile no formal chemical bond is observed between the α-carbon and the nitrogen, as well as between the α-carbon and the oxygen, when the system is around its transition state reaction coordinate (**II**–**IV**).

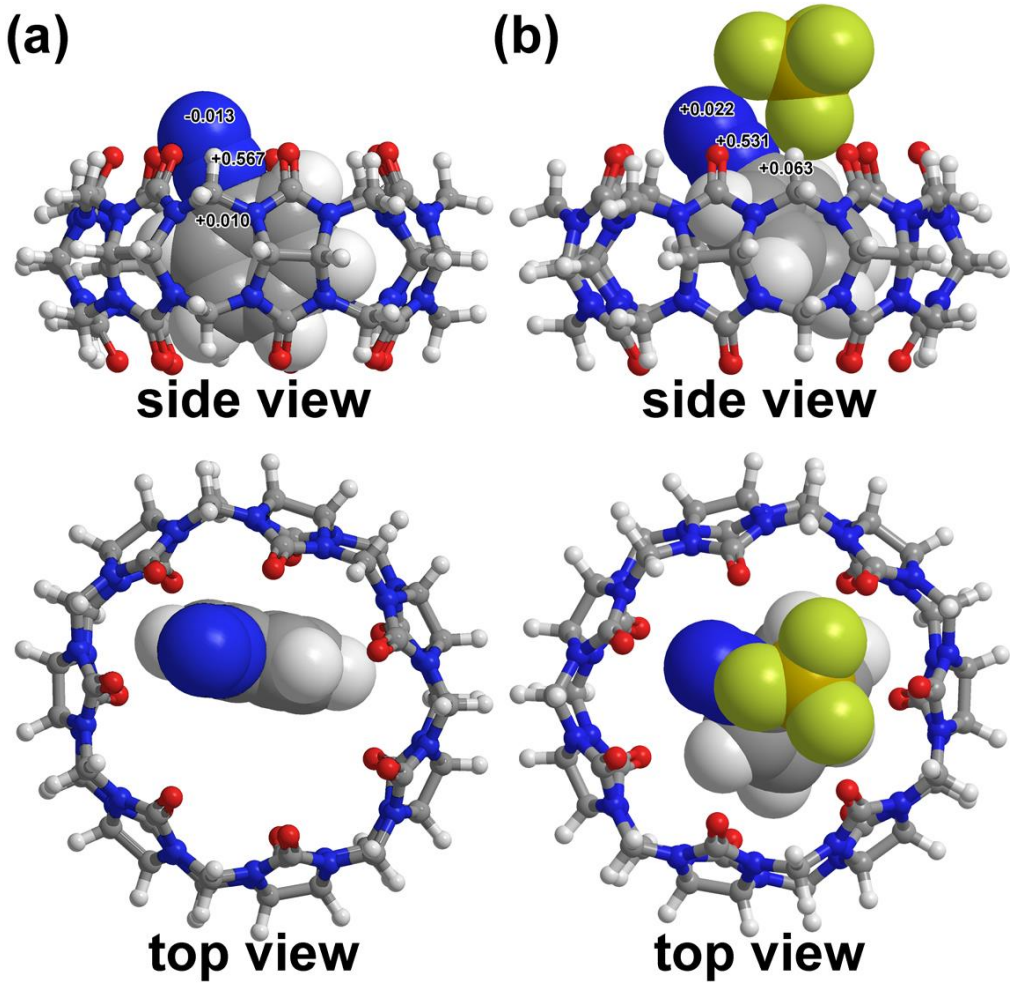

Figure S17. Molecular models of **(a)** $[CB7\text{-}PhN_2]^+$ and **(b)** $[CB7\text{-}PhN_2]^+[BF_4]^-$ optimized at CPCM/wB97XD/6-31G* level of theory. Atomic electrostatic partial charges of the diazonium group and the α-carbon are shown as annotation. The presence of a $[BF_4]^-$ counterion shows insignificant effects on the partial charges around the diazonium group, and therefore is not expected to play any significant role in modulating the reactivity of the CB7-encapsulated $[PhN_2]^+$.

Table S2. Binding energies of $[CB7\text{-}PhN_2]^+$ based on the optimized geometry at the wB97XD/6-31G* level of theory. All methods used the CPCM implicit solvation model in water with the exception of GFN2-xTB which used its own alpb solvation model. All values are in kcal mol^{-1}. DLPNO-CCSD(T) and wB97XD/6-311+G** yield very strong binding energies in agreement with the values obtained with wB97XD/6-31G* which are perhaps overestimates. On the other hand, both GFN2-xTB and PM6D3, which are expected to perform well on supramolecular complexes, find lower estimates for the binding energy. Meanwhile HF/6-311+G** finds a barely negative binding energy, as expected, since it is devoid from explicit van der Waals corrections.

	wB97XD/ 6-31G* [a]	**wB97XD/ 6-311+G** [b]**	**DLPNO-CCSD(T) [c]**	**GFN2-xTB [d]**	**PM6D3 [e]**	**HF/ 6-311+G** [f]**
$[CB7\text{-}PhN_2]^+$	-23.80	-36.53	-32.84	-17.26	-20.75	-0.48

[a] Calculations performed using Gaussian16
[b] Calculations performed using Gaussian16
[c] Calculations performed using Orca 5.0 with LoosePNO settings and the cc-pVTZ, cc-pVTZ/C, def2/J datasets with RIJCOSX approximation
[d] Calculations performed using xTB 6.3.3
[e] Calculations performed using Gaussian16
[f] Calculations performed using Gaussian16

Table S3. Activation energies of the $S_N1(Ar)$ reaction of $[PhN_2\text{-}H_2O]^+$ in CB7 and in an explicit water cage, based on the optimized geometry at wB97XD/6-31G* level of theory. All values are in kcal mol^{-1}. DLPNO-CCSD(T) and wB97XD/6-311+G** are in close agreement with each other and support the wB97XD/6-31G* results. GFN2-xTB and PM6D3 on the other hand vastly overestimate the activation energy and incorrectly predict the sign of $\Delta\Delta H^{\ddagger}$, suggesting that these semi-empirical methods are not optimized for transition state energy calculations.

	wB97XD/ 6-31G* [a]	**wB97XD/ 6-311+G** [b]**	**DLPNO-CCSD(T) [c]**	**GFN2-xTB [d]**	**PM6D3 [e]**
$TS([CB7\text{-}PhN_2\text{-}H_2O]^+)$	31.46	34.10	33.65	54.17	46.91
$TS([(H_2O)_{84}\text{-}[PhN_2\text{-}H_2O]^+)$	28.02	29.85	30.23	57.54	53.31
$\Delta\Delta H^{\ddagger}$ [f]	3.44	4.25	3.42	-3.37	-6.4

[a] Calculations performed using Gaussian16
[b] Calculations performed using Gaussian16
[c] Calculations performed using Orca 5.0 with LoosePNO settings and the cc-pVTZ, cc-pVTZ/C, def2/J datasets with RIJCOSX approximation
[d] Calculations performed using xTB 6.3.3
[e] Calculations performed using Gaussian16
[f] Experimental $\Delta\Delta H^{\ddagger}$ = 2.4 kcal mol^{-1}

S9. Azo dye quantification by UV-vis spectroscopy

The yield of azo dye formed from diazo coupling reactions with 2-naphthol for aged sample solutions of $[PhN_2]^+$ and $[CB7\text{-}PhN_2]^+$ is calculated using the formula below. See Section S1a for experimental protocols of diazo coupling reactions, as well as azo dye extraction and quantification.

$$Yield = \left[\frac{Number\ of\ moles\ of\ extracted\ azo\ dye\ at\ a\ specific\ ageing\ time}{Initial\ number\ of\ moles\ of\ diazonium\ in\ reaction\ mixture\ before\ ageing}\right] X\ 100\ \%$$

Table S4. Yield of azo dye formed from $[PhN_2]^+$ and $[CB7\text{-}PhN_2]^+$ after ageing under dark condition

Ageing time (Days)	Yield of azo dye (%)	
	$[PhN_2]^+$	$[CB7\text{-}PhN_2]^+$
0	94	92
1	6	77
2	4	72
3	3	66
10	0	48
20	0	37
40	0	10
55	0	12
70	0	3

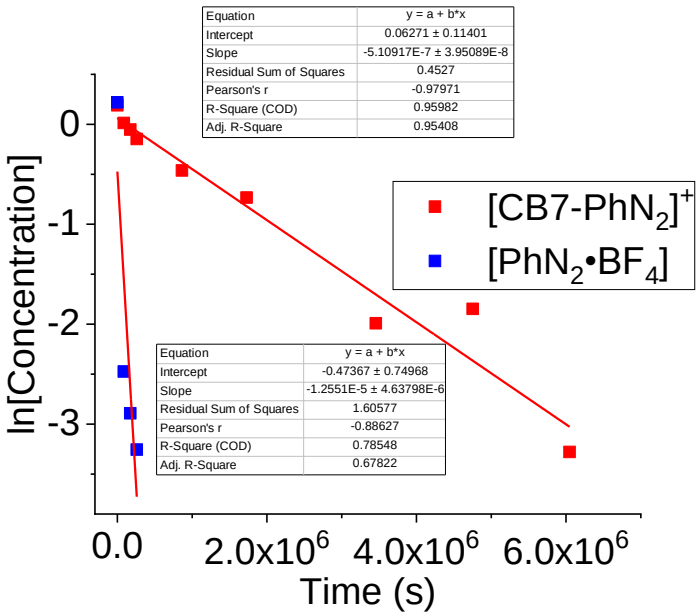

Figure S18. Plots of ln[concentration of extracted azo dye] against time for $[PhN_2]^+$ and $[CB7\text{-}PhN_2]^+$, and the corresponding linear fits with parameters shown in the insets. By assuming the diazo coupling reaction to exhibit quasi-quantitative (i.e. 100%) conversion, rate constants of the decomposition of $[PhN_2]^+$ and $[CB7\text{-}PhN_2]^+$ in water can be estimated by the – slope of the linear fits, which are equal to 1.26 x 10^{-5} s^{-1} for $[PhN_2]^+$ and 5.11 x 10^{-7} s^{-1} for $[CB7\text{-}PhN_2]^+$. These rate constants match very well with those directly determined by ^1H NMR measurement, implying that the above assumption is indeed valid. In other words, the remaining $[CB7\text{-}PhN_2]^+$ in the aged samples are still highly reactive in diazo coupling reaction, despite the reduced concentration.

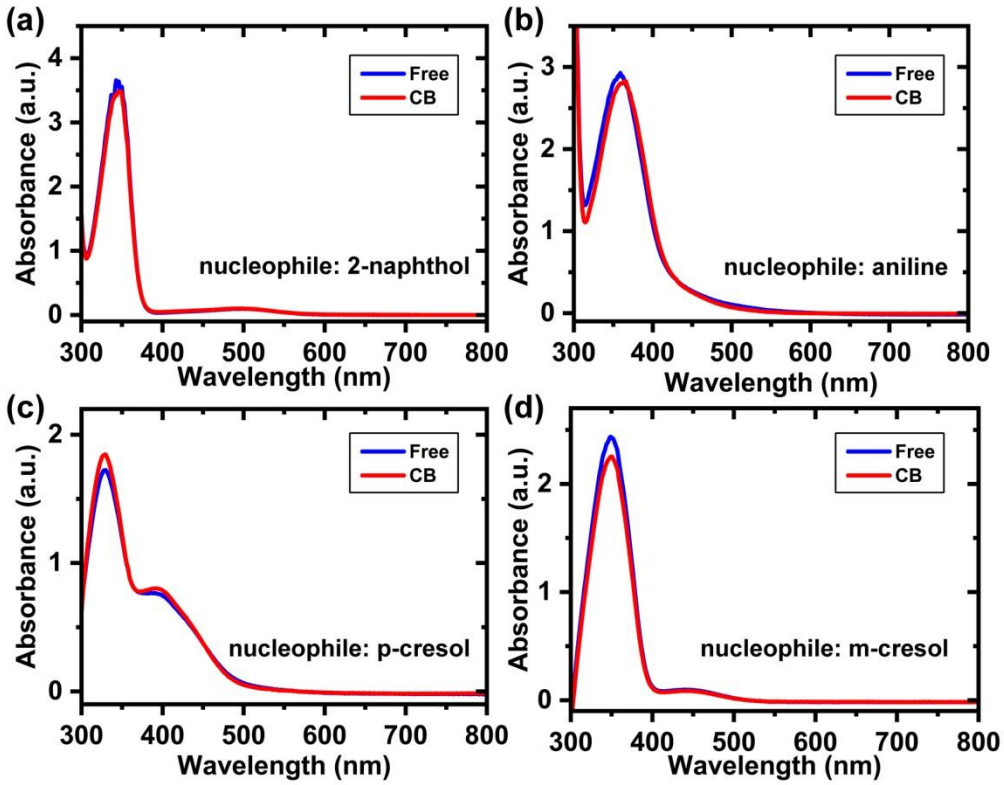

Figure S19. UV-vis spectra of azo dyes prepared by diazo coupling between fresh free $[PhN_2]^+$ (blue curves) or $[CB7\text{-}PhN_2]^+$ (red curves) and a range of nucleophiles, including **(a)** 2-naphthol, **(b)** aniline, **(c)** p-cresol, and **(d)** m-cresol. The diazo coupling reactions were performed at pH = ca. 10 for 2-naphthol and cresol, and at pH = ca. 4 for aniline. In all cases, the as-synthesised azo dyes were extracted by dichloromethane, dried and redissolved in the same volume of dichloromethane to yield a stock solution. For each azo dye, UV-vis samples were prepared by diluting the stock solutions by the same factor. The insignificant difference in absorbance between samples prepared in the presence and the absence of CB7 indicates that the reaction yields are practically the same in the two scenarios. Thus the S_EAr pathway is not hindered after CB7-complexation compared to that of free diazonium ions, illustrating that the observed regioselectivity ($S_N1(Ar)$ vs S_EAr) and its underpinning mechanism are generic across various nucleophilic substrates.

S10. Author Contributions

T.C.L. conceived the project and supervised the solution-phase experiments. E.K. supervised MS experiments and data analysis. S.M. synthesized the molecules, as well as conducted the NMR and MS measurements. A.C.B. performed the UV-vis experiments. T.C.L. and H.L. conducted the computational modelling. All authors contributed to the data analysis and writing of the manuscript. S.M. and A.C.B. contributed equally to this work.

S11. References

S1 W.-H. Huang, S. Liu and L. Isaacs, *Modern Supramolecular Chemistry* (Eds F. Diederich, P. J. Stang, & R. R. Tykwinski) Wiley-VCH, 2008, 113–142.

S2 J. L. Brumaghim, M. Michels, D. Pagliero and K. N. Raymond, *Eur. J. Org. Chem.*, 2004, **24**, 5115–5118.

S3 V. Gabelica, A. A. Shvartsburg, C. Afonso, P. Barran, J. L. P. Benesch, C. Bleiholder, M. T. Bowers, A. Bilbao, M. F. Bush, J. L. Campbell, I. D. G. Campuzano, T. Causon, B. H. Clowers, C. S. Creaser, E. De Pauw, J. Far, F. Fernandez-Lima, J. C. Fjeldsted, K. Giles, M. Groessl, C. J. Hogan Jr, S. Hann, H. I. Kim, R. T. Kurulugama, J. C. May, J. A. McLean, K. Pagel, K. Richardson, M. E. Ridgeway, F. Rosu, F. Sobott, K. Thalassinos, S. J. Valentine and T. Wyttenbach, *Mass Spectrom. Rev.*, 2019, **38**, 291–320.

S4 S. M. Stow, T. J. Causon, X. Zheng, R. T. Kurulugama, T. Mairinger, J. C. May, E. E. Rennie, E. S. Baker, R. D. Smith, J. A. McLean, S. Hann and J. C. Fjeldsted, *Anal. Chem.*, 2017, **89**, 9048–9055.

S5 C. Bannwarth, S. Ehlert and S. Grimme, *J. Chem. Theory Comput.*, 2019, **15**, 1652–1671.

S6 J. G. Brandenburg, C. Bannwarth, A. Hansen and S. Grimme, *J. Chem. Phys.*, 2018, **148**, 064104.

S7 H. Xu and Q. Wang, *Chin. Chem. Lett.*, 2019, **30**, 337–339.

S8 R.-L. Lin, G.-S. Fang, W.-Q. Sun and J.-X. Liu, *Sci. Rep.*, 2016, **6**, 39057.